International Journal for Multiscale Computational Engineering, 16(2):187–207 (2018)

A VARIANT OF THE S-VERSION OF THE FINITE ELEMENT METHOD FOR CONCURRENT MULTISCALE COUPLING

Wei Sun,[1,*] Jacob Fish,[2] & Hachmi Ben Dhia[3]

[1]*State Key Laboratory of Hydroscience and Engineering, Tsinghua University, Beijing 100084, China*

[2]*Civil Engineering and Engineering Mechanics, Columbia University, New York, New York 10027, USA*

[3]*Laboratoire MSSMat, CentraleSupélec, Université Paris-Saclay, UMR CNRS 8579, France*

*Address all correspondence to: Wei Sun, State Key Laboratory of Hydroscience and Engineering, Tsinghua University, Beijing 100084, China; Tel.: +1 212 854 5275; Fax: +1 212 854 6267, E-mail: ws2537@columbia.edu

Original Manuscript Submitted: 4/26/2018; Final Draft Received: 4/26/2018

A variant of the s-version of the finite element method (hereafter coined the s-method) for concurrent multiscale coupling is developed. The proposed method is inspired by a combination of the s-version of the finite element method and the Arlequin method. It features a superposition of a local (fine) mesh, which partly overlaps a global (coarse) mesh, and appropriate homogeneous boundary conditions on both meshes that enforce solution continuity. Its performance in terms of accuracy and computational efficiency in solving a class of multiscale continuum mechanics problems is evaluated by virtue of comparison to the fine reference single mesh and the Arlequin method. Numerical studies are conducted for one-, two-, and three-dimensional problems. For select local and global meshes, the cause of accuracy gains in comparison to the Arlequin method, while having almost the same gain in CPU time, with respect to the discrete single fine mesh for both approaches, is explained.

KEY WORDS: *s-method, Arlequin method, concurrent multiscale, enrichment, coupling, finite element method*

1. INTRODUCTION

Multiscale simulation of materials and structures is one of the research frontiers in the fields of material science and industrial engineering. Computational multiscale approaches can be categorized into hierarchical methods, which can be either one- or two-way coupled, and concurrent methods. The above three methods are aimed at different multiscale issues. In the one-way coupled hierarchical method, the fine-scale information is passed onto coarse scale but not vice versa. Linear computational homogenization and various nonlinear coarse-graining schemes, which focus on determining effective macroscopic properties, fall into the category of one-way coupled hierarchical methods. The two-way coupled hierarchical methods (Fish et al., 1999; Fish, 2013; Feyel, 1999; Guo and Zhao, 2014) repeatedly solve a nonlinear boundary value problem at a fine scale at each coarse-scale quadrature point. Finally, the concurrent multiscale methods are closely related to domain decomposition approaches that either link different mathematical models described by various physics and/or scales or identical mathematical models having distinctly different discretization resolution. Concurrent methods are typically employed to model nonperiodic solutions, such as localized failure. For concurrent methods, linking various mathematical models, such as atomistic and continuum descriptions, the reader is referred to (Fish, 2006, 2007; Xiao and Belytschko, 2004; Xu and Belytschko, 2008; Ben Dhia and Elkhodja, 2007; Bauman et al., 2008).

1543–1649/18/$35.00

Concurrent methods can be further classified based on how solution is decomposed, i.e., enriched or coupled (Duval et al., 2016). Coupling schemes can be either overlapping or coexistent, and the interface (or interphase) can be of the same or lower dimensional manifold (Fish et al., 1999). Finally, the solution approaches can be either iterative or direct (Gendre et al., 2009).

In the enrichment-based concurrent methods, the total solution u is decomposed into coarse-scale u^G and fine-scale correction u^L. A wide range of these methods differ in the approximations of u^G and u^L, the selection of the interface Γ^{GL} and the solution of the global-local system of equations (Fish and Shek, 2000). Among the noteworthy enrichment methods are the variational multiscale method (VMM) (Hughes, 1995), the generalized finite element method (GFEM) (Strouboulis et al., 2000), and the extended FEM (XFEM) (Belytschko and Black, 1999), with the latter two based on the partition of unity method (PUM) (Melenk and Babuška, 1996).

In the concurrent coupling schemes, coupling between subdomains is typically weekly enforced using mortar FEMs (Bernardi et al., 1990a,b; Belgacem, 1999) or the Arlequin framework (Ben Dhia, 1998; Ben Dhia and Rateau, 2005). The Arlequin framework introduces an overlapping region in which the two models are coupled using Lagrange multipliers. The dual coupling has been commented by Ben Dhia (1999) and Ben Dhia et al. (2008). The L^2 norm and the H^1 scalar product coupling operators in the gluing (or interphase) zone have been studied in detail (Ben Dhia and Rateau, 2001, 2005; Ben Dhia, 2008; Guidault and Belytschko, 2007; Sun and Mota, 2014). The penalty operator has also been used (Ben Dhia, 1998; Qiao et al., 2011) and the penalty-duality coupling suggested in (Ben Dhia, 1998). Because of its flexibility in coupling different physics and/or scales, the Arlequin method was adopted in the commercial Code-Aster (Ben Dhia and Rateau, 2002).

Because of the hierarchical decomposition of approximation space, multigrid solvers are well suited for solving enrichment-based concurrent schemes. On the other hand, concurrent coupling schemes are typically solved using finite element tearing and interconnecting (FETI) (Farhat and Roux, 1991; Ben Dhia et al., 2008) and Schwarz alternating methods (Schwarz, 1870; Mota et al., 2017).

The primary objective of the present paper is to study the s-version of the finite element method (Fish, 1992a,b, 1993, 1997; Fan and Fish, 2008; Jiao and Fish, 2015a,b), not as a bubble FE enrichment for which it was originally developed, but as a concurrent coupling scheme based on a FE-enriched junction. To evaluate the efficiency of this variant of the s-method, it is compared in terms of accuracy and computational efficiency to the Arlequin method, widely considered as one of the best concurrent coupling schemes.

The paper is organized as follows: Section 2 briefly reviews the s-method and Arlequin method. The quantitative comparisons in the accuracy and computational efficiency are conducted in Section 3. In Section 4, we discuss the consistency and the modeling errors: the cause in accuracy gains of the s-method, for the considered multiscale continuum mechanics tests, is explained. Concluding remarks are given in Section 5.

2. OVERVIEW OF S-METHOD AND ARLEQUIN METHOD

As a prelude, we start with a brief review of the basic formulations of the s-method and Arlequin method. The point of departure is a variant of the s-method to link two subdomains via partial overlap and homogeneous boundary conditions on the interconnected domains. In the present paper, we consider concurrent coupling under the assumptions of infinitesimal deformation, an isothermal quasi-static state, and material nonlinearity.

In the framework conceived originally by Fish (1992a), the s-method features hierarchical decomposition of the approximation space, i.e., the local mesh is designed as the enrichment to the underlying global mesh. Hence, the crucial local features, such as crack tips or shear bands, are resolved by the superposition mesh (Fish, 1992b). In the present paper, the potential of the s-method is explored for concurrent coupling rather than as an enrichment scheme. By this approach, the superimposed local domain is positioned partly outside the global mesh similarly to the setup considered in the Arlequin method (Ben Dhia and Rateau, 2005) as shown in Fig. 1.

Consider a nonlinear solid occupying an open-bounded regular domain $\Omega \subset R^3$. Its boundary is denoted by $\partial\Omega$, which consists of the prescribed displacement boundary $\partial_u\Omega$ and the prescribed traction boundary $\partial_t\Omega$, such that $\partial\Omega = \partial_u\Omega \cup \partial_t\Omega$ and $\partial_u\Omega \cap \partial_t\Omega = \emptyset$. Let b denote the prescribed body force, $\bar{u}$ the prescribed boundary displacement, $\bar{t}$ the prescribed traction, and n the unit normal to the boundary $\partial_t\Omega$. The domain Ω is partitioned into subdomains Ω^G (coarse mesh representing the global scale) and Ω^L (fine mesh representing the local refinement

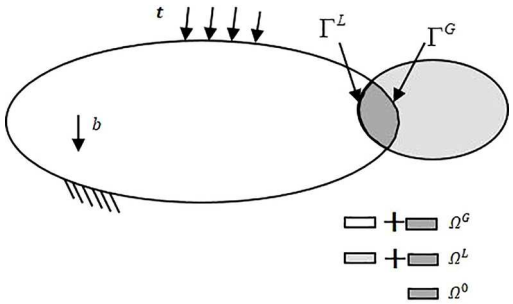

FIG. 1: Two coupling subdomains and the corresponding boundaries

region), such that $\Omega^G \cup \Omega^L = \Omega$ and $\Omega^G \cap \Omega^L = \Omega^0$, where Ω^0 is the coupling or overlap zone. The measure of Ω^0, meas (Ω^0), is such that meas $(\Omega^0) \neq \emptyset$. For $i = G, L$, $\Gamma^i = \partial\Omega^i/(\partial\Omega^i \cap \partial\Omega)$ is the portion of $\partial\Omega^i$ which is not part of $\partial\Omega$. For simplicity, the displacement is imposed on the portion of $\partial_u\Omega^G$ of $\partial\Omega^G \cap \partial\Omega$ and the surface traction is imposed only on the portion of $\partial_t\Omega^G$ of $\partial\Omega^G \cap \partial\Omega$.

We start by considering a weak form without partitioning the problem domain, which states:

Find $u \in \mathcal{U}$ such that

$$a(u, v) = l(v), \forall v \in \mathcal{V} \tag{1}$$

where $\mathcal{U}$, $\mathcal{V}$ are the trial solution and the test function spaces, respectively, defined as follows:

$$\mathcal{U} = \{\, u |\, u \in \mathcal{H}^1(\Omega), \quad u = \bar{u} \quad \text{on} \quad \partial_u\Omega\} \tag{2}$$

$$\mathcal{V} = \{\, v |\, v \in \mathcal{H}^1(\Omega), \quad v = 0 \quad \text{on} \quad \partial_u\Omega\} \tag{3}$$

The internal virtual work is given by the bilinear form

$$a(u, v) = \int_\Omega \sigma(u) : \varepsilon(v) d\Omega \tag{4}$$

whereas, the external virtual work is defined by the linear form

$$l(v) = \int_\Omega v \cdot b d\Omega + \int_{\partial_s\Omega} v \cdot \bar{t} d\Gamma \tag{5}$$

The constitutive equation is denoted as follows:

$$\sigma = \sigma(\varepsilon(u), \xi) \quad \text{in} \quad \Omega \tag{6}$$

where ξ denotes internal state variables.

We refer to the exact solution of a single domain model (1) as the exact solution, denoted herein as u^*.

2.1 S-Method

In the variant of the s-method considered herein, the displacement is decomposed into the coarse-scale or global mesh u^G and the fine-scale or local mesh u^L. Homogeneous boundary conditions are imposed to maintain C^0 continuity as described below. The displacements in different subdomains are defined as follows:

$$\boldsymbol{u} = \begin{cases} \boldsymbol{u}^G & \text{in} \quad \Omega^G/(\Omega^0) \\ \boldsymbol{u}^G + \boldsymbol{u}^L & \text{in} \quad \Omega^0 \\ \boldsymbol{u}^L & \text{in} \quad \Omega^L/(\Omega^0) \end{cases} \tag{7}$$

with the following homogeneous boundary conditions:

$$\begin{array}{l} u^L = 0 \quad \text{on} \quad \Gamma^L \\ u^G = 0 \quad \text{on} \quad \Gamma^G \end{array} \tag{8}$$

Assuming the displacements and surface traction are imposed only on $\partial\Omega^G \cap \partial\Omega$, the trial solution and the test function spaces are defined as follows:

$$\mathcal{U}^G = \{ u^G \big|\, u^G \in \mathcal{H}^1(\Omega^G), u^G = \bar{u} \quad \text{on} \quad \partial_u\Omega^G, u^G = 0 \quad \text{on} \quad \Gamma^G \} \tag{9}$$

$$\mathcal{V}^G = \{ v^G \big|\, v^G \in \mathcal{H}^1(\Omega^G), v^G = 0 \quad \text{on} \quad \Gamma^G \cup \partial_u\Omega^G \} \tag{10}$$

$$\mathcal{U}^L = \{ u^L \big|\, u^L \in \mathcal{H}^1(\Omega^L), u^L = 0 \quad \text{on} \quad \Gamma^L \} \tag{11}$$

$$\mathcal{V}^L = \{ v^L \big|\, v^L \in \mathcal{H}^1(\Omega^L), v^L = 0 \quad \text{on} \quad \Gamma^L \} \tag{12}$$

The test functions, similarly to the trial solution, in $\Omega^G \cap \Omega^L$ are decomposed as follows:

$$v = v^G + v^L \tag{13}$$

Assuming infinitesimal deformation, the strains are linearly decomposed as follows:

$$\varepsilon = \varepsilon^G + \varepsilon^L \tag{14}$$

$$\varepsilon(v) = \varepsilon(v^G) + \varepsilon(v^L) \tag{15}$$

Let us define the following weak problem:
Find $(u^G, u^L) \in \mathcal{U}^G \times \mathcal{U}^L$ such that

$$\begin{array}{c} \forall (v^G, v^L) \in \mathcal{V}^G \times \mathcal{V}^L \\ a^S(u^G + u^L, v^G + v^L) = l^S(v^G + v^L) \end{array} \tag{16}$$

where

$$\begin{aligned} a^S(u^G + u^L, v^G + v^L) = & \int_{\Omega^0} \sigma(u^G + u^L) : \varepsilon(v^G + v^L) d\Omega \\ & + \int_{\Omega^G/\Omega^0} \sigma(u^G) : \varepsilon(v^G) d\Omega + \int_{\Omega^L/\Omega^0} \sigma(u^L) : \varepsilon(v^L) d\Omega \end{aligned} \tag{17}$$

$$l^S(v^G + v^L) = \int_{\Omega^G} v^G \cdot b d\Omega + \int_{\Omega^L} v^L \cdot b d\Omega + \int_{\partial_s\Omega^G} v^G \cdot \bar{t} d\Gamma \tag{18}$$

We next introduce the spatial discretization for the primary fields and test functions as follows:

$$u_i^G = N_{i\alpha}^G d_\alpha^G \in (\mathcal{U}^G)^h, \quad v_i^G = N_{i\beta}^G c_\beta^G \in (\mathcal{V}^G)^h \tag{19}$$

$$u_i^L = N_{i\Lambda}^L d_\Lambda^L \in (\mathcal{U}^L)^h, \quad v_i^L = N_{i\Pi}^L c_\Pi^L \in (\mathcal{V}^L)^h \tag{20}$$

where $(\mathcal{U}^G)^h \subset \mathcal{U}^G$, $(\mathcal{U}^L)^h \subset \mathcal{U}^L$, $(\mathcal{V}^G)^h \subset \mathcal{V}^G$, and $(\mathcal{V}^L)^h \subset \mathcal{V}^L$ are finite-dimensional subspaces spanned by the corresponding interpolation functions; $i = 1, K, n_{sd}$, where n_{sd} denotes the number of space dimensions; $N_{i\beta}^G$ and $N_{i\Pi}^L$ are C^0 continuous shape functions of the coarse and fine meshes, respectively; $(\alpha, \beta) = 1, K, N_{\text{dof}}^G$, where N_{dof}^G denotes the number of degrees of freedom in the coarse mesh Ω^G; $(\Lambda, \Pi) = 1, K, n_{\text{dof}}^L$, where n_{dof}^L denotes the number of degrees of freedom in the fine mesh Ω^L; d^G is the vector of nodal displacements of the coarse mesh and its components corresponding to nodal points on $\Gamma^G \cup \partial_u\Omega^G$ should satisfy the prescribed kinematic constrains; c^G is the vector of virtual nodal displacements in the coarse mesh and its components associated with nodal points

belonging to $\Gamma^G \cup \partial_u \Omega^G$ must vanish in accordance with the definition of $\mathcal{V}^G$; and d^L, c^L are the vectors of nodal displacements and virtual nodal displacements in the fine mesh, respectively.

The discretized global and local strains are given by

$$\varepsilon_{ij}^G = B_{ij\alpha}^G d_\alpha^G, \varepsilon_{ij}^L = B_{ij\Lambda}^L d_\Lambda^L \tag{21}$$

where

$$\begin{aligned} B_{ij\alpha}^G &= \frac{1}{2}\left(\frac{\partial N_{i\alpha}^G}{\partial x_j} + \frac{\partial N_{j\alpha}^G}{\partial x_i}\right) \\ B_{ij\Lambda}^L &= \frac{1}{2}\left(\frac{\partial N_{i\Lambda}^L}{\partial x_j} + \frac{\partial N_{j\Lambda}^L}{\partial x_i}\right) \end{aligned} \tag{22}$$

Substituting the discrete form in (19)–(22) into (16) yields

$$r_\alpha^G = f_\alpha^{\text{int},G} - f_\alpha^{\text{ext},G} = 0 \tag{23}$$

$$r_\Lambda^L = f_\Lambda^{\text{int},L} - f_\Lambda^{\text{ext},L} = 0 \tag{24}$$

where

$$f_\alpha^{\text{int},G} = \int_{\Omega^0} B_{ij\alpha}^G \sigma_{ij}(\varepsilon(\boldsymbol{d}), \xi) d\Omega + \int_{\Omega^G/\Omega^0} B_{ij\alpha}^G \sigma_{ij}^G(\varepsilon(\boldsymbol{d}^G), \xi^G) d\Omega \tag{25}$$

$$f_\alpha^{\text{ext},G} = \int_{\Omega^G} N_{i\alpha}^G b_i d\Omega + \int_{\partial_s \Omega^G} N_{i\alpha}^G \bar{t}_i d\Gamma \tag{26}$$

$$f_\Lambda^{\text{int},L} = \int_{\Omega^0} B_{ij\Lambda}^L \sigma_{ij}(\varepsilon(\boldsymbol{d}), \xi) d\Omega + \int_{\Omega^L/\Omega^0} B_{ij\Lambda}^L \sigma_{ij}^L(\varepsilon(\boldsymbol{d}^L), \xi^L) d\Omega \tag{27}$$

$$f_\Lambda^{\text{ext},L} = \int_{\Omega^L} N_{i\Lambda}^L b_i d\Omega \tag{28}$$

Because only material nonlinearity is considered, the linearized incremental equations yield the tangent stiffness matrix

$$\boldsymbol{K} = \begin{bmatrix} \boldsymbol{K}^{GG} & \boldsymbol{K}^{GL} \\ \boldsymbol{K}^{LG} & \boldsymbol{K}^{LL} \end{bmatrix} \tag{29}$$

where submatrices in (29) expressed in the indicial notation are given by

$$K_{\alpha\beta}^{GG} = \frac{\partial r_\alpha^G}{\partial d_\beta^G} = \int_{\Omega^G} B_{ij\alpha}^G L_{ijkl} B_{kl\beta}^G d\Omega \tag{30}$$

$$K_{\Lambda\Pi}^{LL} = \frac{\partial r_\Lambda^L}{\partial d_\Pi^L} = \int_{\Omega^L} B_{ij\Lambda}^L L_{ijkl} B_{kl\Pi}^L d\Omega \tag{31}$$

$$K_{\alpha\Pi}^{GL} = \frac{\partial r_\alpha^G}{\partial d_\Pi^L} = \int_{\Omega^0} B_{ij\alpha}^G L_{ijkl} B_{kl\Pi}^L d\Omega \tag{32}$$

and

$$L_{ijkl} = \frac{\partial \sigma_{ij}}{\partial \varepsilon_{kl}} \tag{33}$$

2.2 Arlequin Method

In the Arlequin method, a partition of unity of the parameters functions, representing an appropriately chosen relative weight for each model in the overlap, and Lagrange multipliers, are introduced to enforce weak compatibility between the two subdomains, where the global and local models are defined, respectively.

To define the Arlequin weak form, we introduce the trial solution and the test function spaces of the coarse and fine fields as follows:

$$\mathcal{U}^G = \{\, \boldsymbol{u}^G \big|\, \boldsymbol{u}^G \in \mathcal{H}^1(\Omega^G), \boldsymbol{u}^G = \bar{\boldsymbol{u}} \quad \text{on} \quad \partial_u \Omega^G \} \tag{34}$$

$$\mathcal{V}^G = \{\, \boldsymbol{v}^G \big|\, \boldsymbol{v}^G \in \mathcal{H}^1(\Omega^G), \boldsymbol{v}^G = 0 \quad \text{on} \quad \partial_u \Omega^G \} \tag{35}$$

$$\mathcal{U}^L = \{\, \boldsymbol{u}^L \big|\, \boldsymbol{u}^L \in \mathcal{H}^1(\Omega^L) \} \tag{36}$$

$$\mathcal{V}^L = \{\, \boldsymbol{v}^L \big|\, \boldsymbol{v}^L \in \mathcal{H}^1(\Omega^L) \} \tag{37}$$

By theoretical arguments, the Lagrange multiplier is to be sought in the dual space of $\mathcal{H}^1(\Omega^0)$. But for practical reasons and by using mathematical classical results, the Lagrange multiplier is represented in the (primal) space $\mathcal{H}^1(\Omega^0)$. Thus, its trial solution and the test function spaces can be defined as: (see, Ben Dhia, 2008)

$$\mathcal{U}^\lambda = \{\, \boldsymbol{\lambda} \big|\, \boldsymbol{\lambda} \in \mathcal{H}^1(\Omega^0) \} \tag{38}$$

$$\mathcal{V}^\lambda = \{\, \boldsymbol{v}_\lambda \big|\, \boldsymbol{v}_\lambda \in \mathcal{H}^1(\Omega^0) \} \tag{39}$$

The weak form of the problem is then described as follows:
Find $(\boldsymbol{u}^G, \boldsymbol{u}^L, \boldsymbol{\lambda}) \in \mathcal{U}^G \times \mathcal{U}^L \times \mathcal{U}^\lambda$, such that

$$\begin{gathered} \forall (\boldsymbol{v}^G, \boldsymbol{v}^L, \boldsymbol{v}^\lambda) \in \mathcal{V}^G \times \mathcal{V}^L \times \mathcal{V}^\lambda \\ \begin{cases} a^G(\boldsymbol{u}^G, \boldsymbol{v}^G) + C(\boldsymbol{\lambda}, \boldsymbol{v}^G) = l^G(\boldsymbol{v}^G) \\ a^L(\boldsymbol{u}^L, \boldsymbol{v}^L) - C(\boldsymbol{\lambda}, \boldsymbol{v}^L) = l^L(\boldsymbol{v}^L) \\ C(\boldsymbol{v}^\lambda, \boldsymbol{u}^G - \boldsymbol{u}^L) = 0 \end{cases} \end{gathered} \tag{40}$$

where the bilinear and linear forms are defined as follows

$$a^G(\boldsymbol{u}^G, \boldsymbol{v}^G) = \int_{\Omega^G} \alpha^G \boldsymbol{\sigma}(\boldsymbol{u}^G, \boldsymbol{\xi}^G) : \boldsymbol{\varepsilon}(\boldsymbol{v}^G) d\Omega \tag{41}$$

$$a^L(\boldsymbol{u}^L, \boldsymbol{v}^L) = \int_{\Omega^L} \alpha^L \boldsymbol{\sigma}(\boldsymbol{u}^L, \boldsymbol{\xi}^L) : \boldsymbol{\varepsilon}(\boldsymbol{v}^L) d\Omega \tag{42}$$

$$l^G(\boldsymbol{v}^G) = \int_{\Omega^G} \beta^G \boldsymbol{v}^G \cdot \boldsymbol{b} d\Omega + \int_{\partial_s \Omega^G} \beta^G \boldsymbol{v}^G \cdot \bar{\boldsymbol{t}} d\Gamma \tag{43}$$

$$l^L(\boldsymbol{v}^L) = \int_{\Omega^L} \beta^L \boldsymbol{v}^L \cdot \boldsymbol{b} d\Omega \tag{44}$$

The coupling operators C based on the H^1 coupling are defined by

$$C(\boldsymbol{u}, \boldsymbol{v}) = \int_{\Omega^0} [\boldsymbol{u} \cdot \boldsymbol{v} + l^2 \boldsymbol{\varepsilon}(\boldsymbol{u}) : \boldsymbol{\varepsilon}(\boldsymbol{v})] d\Omega \tag{45}$$

where l represents the characteristic dimension of the coupling zone Ω^0 and l has units of a length. Herein, l is assumed to be equal to the characteristic size of the fine mesh.

The energy partition depends on the parameters α^G, α^L, which that satisfy

$$\begin{cases} \alpha^G = 1 & \text{in} \quad \Omega^G/(\Omega^0) \\ \alpha^L = 1 & \text{in} \quad \Omega^0 \\ \alpha^G + \alpha^L = 1 & \text{in} \quad \Omega^L/(\Omega^0) \end{cases} \tag{46}$$

The external work parameters β^G, β^L are not necessarily identical to α^G, α^L. Nevertheless, herein we select $\beta^G = \alpha^G$, $\beta^L = \alpha^L$ in the numerical examples.

The spatial discretization for the primary fields and test functions is defined as follows:

$$u_i^G = N_{i\alpha}^G d_\alpha^G \in (\mathcal{U}^G)^h, \quad v_i^G = N_{i\beta}^G c_\beta^G \in (\mathcal{V}^G)^h \tag{47}$$

$$u_i^L = N_{i\Lambda}^L d_\Lambda^L \in (\mathcal{U}^L)^h, \quad v_i^L = N_{i\Pi}^L c_\Pi^L \in (\mathcal{V}^L)^h \tag{48}$$

$$\lambda_i = N_{iA}^\lambda d_A^\lambda \in (\mathcal{U}^\lambda)^h, \quad v_i^\lambda = N_{iS}^\lambda c_S^\lambda \in (\mathcal{V}^\lambda)^h \tag{49}$$

where $(\mathcal{U}^G)^h \subset \mathcal{U}^G$, $(\mathcal{U}^L)^h \subset \mathcal{U}^L$, $(\mathcal{U}^\lambda)^h \subset \mathcal{U}^\lambda$, $(\mathcal{V}^G)^h \subset \mathcal{V}^G$, $(\mathcal{V}^L)^h \subset \mathcal{V}^L$, and $(\mathcal{V}^\lambda)^h \subset \mathcal{V}^\lambda$ are finite-dimensional subspaces spanned by the corresponding interpolation functions; $N_{i\alpha}^G$ and $N_{i\Lambda}^L$ are the usual C^0 continuous shape functions in Ω^G, Ω^L, respectively. Herein, we follow commonly employed approach in Arlequin [see (Ben Dhia and Rateau, (2001) and Guidault and Belytschko, (2007)] by which N_{iA}^λ is C^0 continuous shape functions on Ω^0. $(\alpha, \beta) = 1, K$, n_{dof}^G; $(\Lambda, \Pi) = 1, K$, n_{dof}^L; $(A, S) = 1, K$, n_{dof}^λ; where n_{dof}^G, n_{dof}^L, and n_{dof}^λ denote the corresponding number of degrees of freedom, respectively; $\boldsymbol{d}^G$, $\boldsymbol{d}^L$, and $\boldsymbol{d}^\lambda$ are the vectors of nodal values of the primary fields and $\boldsymbol{c}^G$, $\boldsymbol{c}^L$, and $\boldsymbol{c}^\lambda$ are the corresponding virtual nodal values, respectively.

Assuming infinitesimal deformation, the strain reads as follows:

$$\varepsilon_{ij}^G = B_{ij\alpha}^G d_\alpha^G, \varepsilon_{ij}^L = B_{ij\Lambda}^L d_\Lambda^L, \varepsilon_{ij}^\lambda = B_{ijA}^\lambda d_A^\lambda \tag{50}$$

where

$$\begin{aligned} B_{ij\alpha}^G &= \frac{1}{2}\left(\frac{\partial N_{i\alpha}^G}{\partial x_j} + \frac{\partial N_{j\alpha}^G}{\partial x_i}\right) \\ B_{ij\Lambda}^L &= \frac{1}{2}\left(\frac{\partial N_{i\Lambda}^L}{\partial x_j} + \frac{\partial N_{j\Lambda}^L}{\partial x_i}\right) \\ B_{ijA}^\lambda &= \frac{1}{2}\left(\frac{\partial N_{iA}^\lambda}{\partial x_j} + \frac{\partial N_{jA}^\lambda}{\partial x_i}\right) \end{aligned} \tag{51}$$

Substituting the above spatial discretizations into the weak form (40) yields

$$r_\alpha^G = \alpha^G f_\alpha^{\text{int,G}} - \beta^G f_\alpha^{\text{ext,G}} + C_{\alpha S}^{G\lambda} d_S^\lambda = 0 \tag{52}$$

$$r_\Lambda^L = \alpha^L f_\Lambda^{\text{int},L} - \beta^L f_\Lambda^{\text{ext},L} - C_{\Lambda S}^{L\lambda} d_S^\lambda = 0 \tag{53}$$

$$r_A^\lambda = C_{A\beta}^{G\lambda} d_\beta^G - C_{A\Pi}^{L\lambda} d_\Pi^L = 0 \tag{54}$$

where

$$f_\alpha^{\text{int,G}} = \int_{\Omega^G} B_{ij\alpha}^G \sigma_{ij}^G(\boldsymbol{\varepsilon}(\boldsymbol{d}^G), \boldsymbol{\xi}^G) d\Omega \tag{55}$$

$$f_\alpha^{\text{ext},G} = \int_{\Omega^G} N_{i\alpha}^G b_i d\Omega + \int_{\partial_s \Omega^G} N_{i\alpha}^G \bar{t}_i d\Gamma \tag{56}$$

$$f_\Lambda^{\text{int},L} = \int_{\Omega^L} B_{ij\Lambda}^L \sigma_{ij}^L(\boldsymbol{\varepsilon}(\boldsymbol{d}^L), \boldsymbol{\xi}^L) d\Omega \tag{57}$$

$$f_{\Lambda}^{\text{ext},L} = \int_{\Omega^L} N_{i\Lambda}^L b_i d\Omega \tag{58}$$

$$C_{\alpha S}^{G\lambda} = \int_{\Omega^0} (N_{i\alpha}^G \cdot N_{iS}^{\lambda} + l^2 B_{ij\alpha}^G \cdot B_{ijS}^{\lambda}) d\Omega \tag{59}$$

$$C_{\Lambda S}^{L\lambda} = \int_{\Omega^0} (N_{i\Lambda}^L \cdot N_{iS}^{\lambda} \cdot + l^2 B_{ij\Lambda}^L \cdot B_{ijS}^{\lambda}) d\Omega \tag{60}$$

Considering material nonlinearity only, linearization of the residuals yields the tangent stiffness matrix given by

$$\boldsymbol{K} = \begin{bmatrix} \alpha^G \boldsymbol{K}^{GG} & 0 & \boldsymbol{C}^{G\lambda} \\ 0 & \alpha^L \boldsymbol{K}^{LL} & -\boldsymbol{C}^{L\lambda} \\ (\boldsymbol{C}^{G\lambda})^T & -(\boldsymbol{C}^{L\lambda})^T & 0 \end{bmatrix} \tag{61}$$

where submatrices in (61) expressed in the indicial notation are given by

$$K_{\alpha\beta}^{GG} = \frac{\partial r_{\alpha}^G}{\partial d_{\beta}^G} = \int_{\Omega^G} B_{ij\alpha}^G L_{ijkl}^G B_{kl\beta}^G d\Omega \tag{62}$$

$$K_{\Lambda\Pi}^{LL} == \frac{\partial r_{\Lambda}^L}{\partial d_{\Pi}^L} = \int_{\Omega^L} B_{ij\Lambda}^L L_{ijkl}^L B_{kl\Pi}^L d\Omega \tag{63}$$

and

$$L_{ijkl}^G = \frac{\partial \sigma_{ij}^G}{\partial \varepsilon_{kl}^G}, \quad L_{ijkl}^L = \frac{\partial \sigma_{ij}^L}{\partial \varepsilon_{kl}^L} \tag{64}$$

Remark 1. *The classical displacement continuity $\boldsymbol{u}^G - \boldsymbol{u}^L = 0$ in the L^2 weak sense can be seen as Eq. (65), while the H^1 coupling weakly enforces $(\boldsymbol{u}^G - \boldsymbol{u}^L) - l^2\Delta(\boldsymbol{u}^G - \boldsymbol{u}^L) = 0$.*

$$C(\boldsymbol{u}, \boldsymbol{v}) = \int_{\Omega^0} \boldsymbol{u} \cdot \boldsymbol{v} d\Omega \tag{65}$$

As a matter of fact, the L^2 coupling leads to an ill-posed continuous Arlequin problem but can be given a sense in the discretized Arlequin problem (Ben Dhia, 2008).

3. QUANTITATIVE COMPARISONS BETWEEN THE TWO METHODS

In this section, the accuracy and computational efficiency of the two methods are compared quantitatively.

3.1 One-Dimensional Model Problem

In this example, a one-dimensional model problem of an elastic bar ($EA = \rho g = 1, L = 11$) is considered. The meshes for the s-method and Arlequin method are depicted in Fig. 2.

The error in the energy norm is computed with respect to a reference fine mesh. The error in the energy norm is defined as follows:

$$\|e\| = \sqrt{\int_{\Omega^L} (\boldsymbol{\varepsilon}^{ref} - \boldsymbol{\varepsilon})^T : \mathbb{L} : (\boldsymbol{\varepsilon}^{ref} - \boldsymbol{\varepsilon}) d\Omega} \tag{66}$$

The relative error in energy norm is

$$\eta = \frac{\|e\|}{\|u\|} = \frac{\sqrt{\int_{\Omega^L} (\boldsymbol{\varepsilon}^{ref} - \boldsymbol{\varepsilon})^T : \mathbb{L} : (\boldsymbol{\varepsilon}^{ref} - \boldsymbol{\varepsilon}) d\Omega}}{\sqrt{\int_{\Omega^L} (\boldsymbol{\varepsilon}^{ref})^T : \mathbb{L} : (\boldsymbol{\varepsilon}^{ref}) d\Omega}} \tag{67}$$

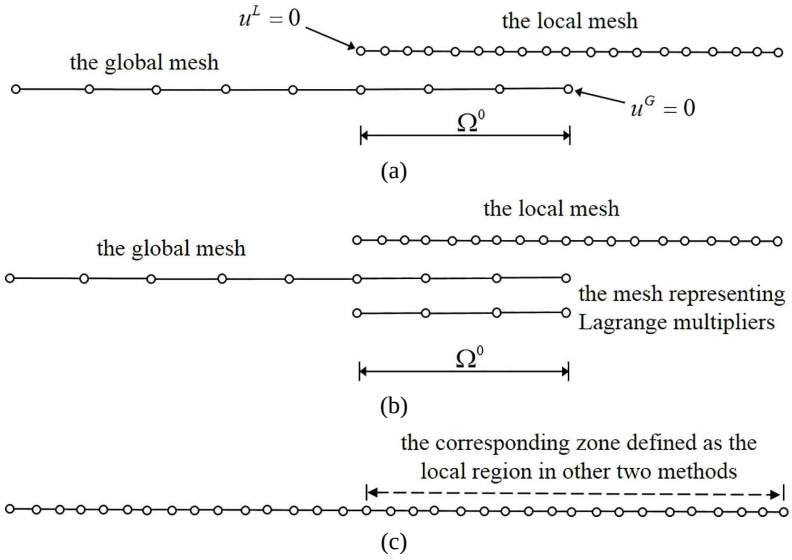

FIG. 2: Finite element meshes for the s-method (a), Arlequin method (b), and reference fine solution (c)

where ε^{ref} and ε are strains obtained by the reference fine mesh and one of the coupling schemes (the s-method or Arlequin method), respectively.

The body force is defined as follows:

$$b(x) = \sin\left[\frac{2\pi}{T}(x-5)\right] \quad (5 \leqslant x \leqslant 11) \tag{68}$$

is applied in the local mesh. Relative errors in the energy norm of the and s-method and Arlequin (with linear continuous function) method are shown in Fig. 3.

It is observed that the relative error in the energy norm of the s-method is lower than in the Arlequin method for all load frequencies considered. As the load period T increases, the errors of the two methods reach an asymptotic value.

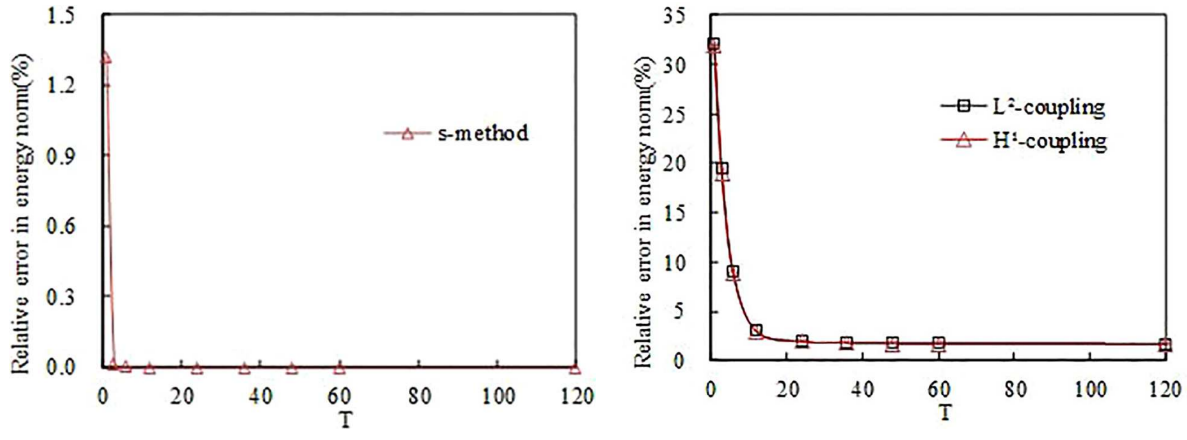

FIG. 3: Relative error in the energy norm of the (a) the s-method and (b) the Arlequin method

3.2 2D-2D Coupling for Fracture Analysis

Herein, we consider a plate with a crack subjected to tensile and shear loadings, respectively (Fig. 4). The problem has been studied by Guidault and Belytschko (2007) in the context of the Arlequin method. A plane strain condition is considered. Material parameters are $E = 2 \times 10^5$ MPa and $\upsilon = 0.3$. The geometry parameters are: $a = 3.5$ mm, $L = 16$ mm, and $w = 7$ mm (see Fig. 4 for definition). Figure 5 depicts the meshes (for the global domain discretization, but only shows the mesh in the coupling zone) used in the coupling schemes. In the Arlequin method, the Lagrange multiplier field and the coarse fields are spanned by the same set of basis functions.

The analytical values of the stress intensity factors SIF are as follows:

- Tensile loading (pure mode I): $K_{\mathrm{I}}^0 = 9.3721$ MPa mm$^{1/2}$.
- Shear loading (mixed mode II): $K_{\mathrm{I}}^0 = 34.00$ MPa mm$^{1/2}$ and $K_{\mathrm{II}}^0 = 4.55$ MPa mm$^{1/2}$.

The extraction of the SIF is obtained using J-integrals. The normalized errors obtained from various approaches are summarized in Tables 1 and 2. It can be seen that the s-method leads to consistently more accurate results. Among the various coupling schemes in the Arlequin method, the L^2 coupling and the H^1 coupling with linear weighting functions give rise to higher accuracy, which is consistent with observations made in Guidault and Belytschko (2007).

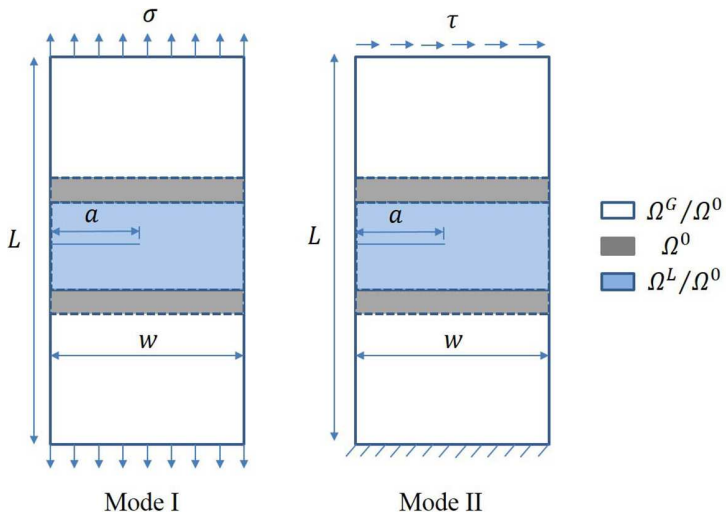

FIG. 4: Structure with a traction-free crack in pure mode I (tensile loading, $\sigma = 1$ MPa) and in mixed mode II (shear loading, $\tau = 1$ MPa); computational conditions of the two methods

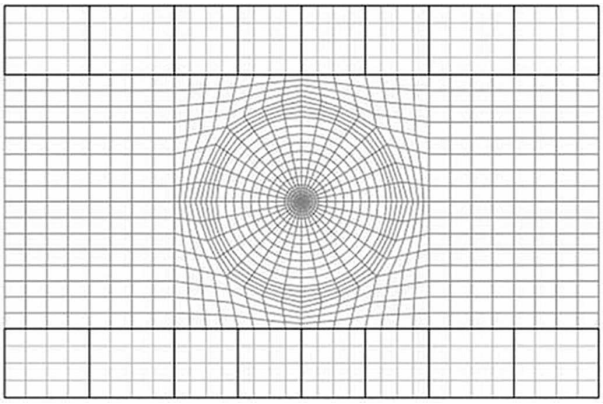

FIG. 5: Fine mesh for Ω^L and coarse mesh for Ω^G (thick line, only shows the coupling zone) using in the coupling schemes

TABLE 1: Mode I case: value and normalized value of the stress intensity factor

—	Fine	s-Method	Arlequin			
			H^1-linear	H^1-constant (0.99)	H^1-constant (0.5)	L^2-linear
$\lvert(K_{\mathrm{I}} - K_{\mathrm{I}}^0)/K_{\mathrm{I}}^0\rvert \times 100\%$	0.001	0.108	0.150	0.436	0.703	0.236

TABLE 2: Mixed mode II case: value and normalized value of the stress intensity factors

—	Fine	s-Method	Arlequin			
			H^1-linear	H^1-constant (0.99)	H^1-constant (0.5)	L^2-linear
$\lvert(K_{\mathrm{I}} - K_{\mathrm{I}}^0)/K_{\mathrm{I}}^0\rvert \times 100\%$	0	0.118	0.176	2.471	2.176	0.235
$\lvert(K_{\mathrm{II}} - K_{\mathrm{II}}^0)/K_{\mathrm{II}}^0\rvert \times 100\%$	0.132	0.154	0.198	0.022	0.176	0.198

We now study the normalized local error in the energy norm defined as follows:

$$\eta^{e,L} = \frac{||\boldsymbol{u} - \boldsymbol{u}_{\text{ref}}||_{\Omega^{e,L}}}{||\boldsymbol{u}_{\text{ref}}||_{\Omega^L}} \tag{69}$$

where $\boldsymbol{u}_{\text{ref}}$ and $\boldsymbol{u}$ are displacements in the reference fine mesh and one of the coupling schemes, $\Omega^{e,L}$ denotes element domains in Ω^L and

$$||\boldsymbol{u}||_{\Omega} = \sqrt{\frac{1}{\text{meas}(\Omega)} \int_{\Omega} \boldsymbol{\varepsilon}(\boldsymbol{u}) : \mathbb{L} : \boldsymbol{\varepsilon}(\boldsymbol{u}) d\Omega} \tag{70}$$

The total values $\sum_{\Omega^L} \eta^{e,L}$ and $\sum_{\Omega^L/\Omega^0} \eta^{e,L}$ are summarized in Table 3. The distributions of the local errors are depicted in Figs. 6 and 7. The distribution of local errors is consistent with previous observations suggesting higher accuracy of the s-method and superior performance of linear weighting functions in the Arlequin method.

3.3 3D-3D Large-Scale Nonlinear Coupling

Herein, we consider an earth-rockfill dam with a small-scale cutoff wall buried in the deep overburden. Figure 8 depicts the maximum cross section and longitudinal profile of the dam. The height of the dam is 200 m, and the depth of the overburden is 100 m; the thickness of the cutoff wall is 1.2 m. The length of the cutoff wall is 63 m, where 60 m is in the overburden. The normal pool level is 190 m. The soil, core, overburden, thin-layer, and high plastic clay are all modeled using the Duncan-ev model (Duncan and Zhang, 1970), and the cutoff wall is modeled using ideal elastic-plastic Mohr-Coulomb model. Material parameters are listed in Table 4. The meshes for various methods are depicted in Fig. 9. The fine and coarse mesh without any coupling are also considered as a reference solution. The H^1 coupling with constant weighting functions ($\alpha^L = 0.99$) and the coarse mediator space for Lagrange multipliers are employed for the Arlequin method.

TABLE 3: Total relative errors in local region

—	—	s-Method	Arlequin			
			H^1-linear	H^1-constant (0.99)	H^1-constant (0.5)	L^2-linear
Mode I Case	$\sum_{\Omega^{\mathrm{L}}} \eta^{\mathrm{e,L}}$	0.165	0.251	0.648	0.724	0.271
	$\sum_{\Omega^{\mathrm{L}}/\Omega^0} \eta^{\mathrm{e,L}}$	0.041	0.057	0.135	0.215	0.072
Mixed Mode II Case	$\sum_{\Omega^{\mathrm{L}}} \eta^{\mathrm{e,L}}$	0.189	0.298	0.731	0.816	0.314
	$\sum_{\Omega^{\mathrm{L}}/\Omega^0} \eta^{\mathrm{e,L}}$	0.039	0.063	0.164	0.255	0.074

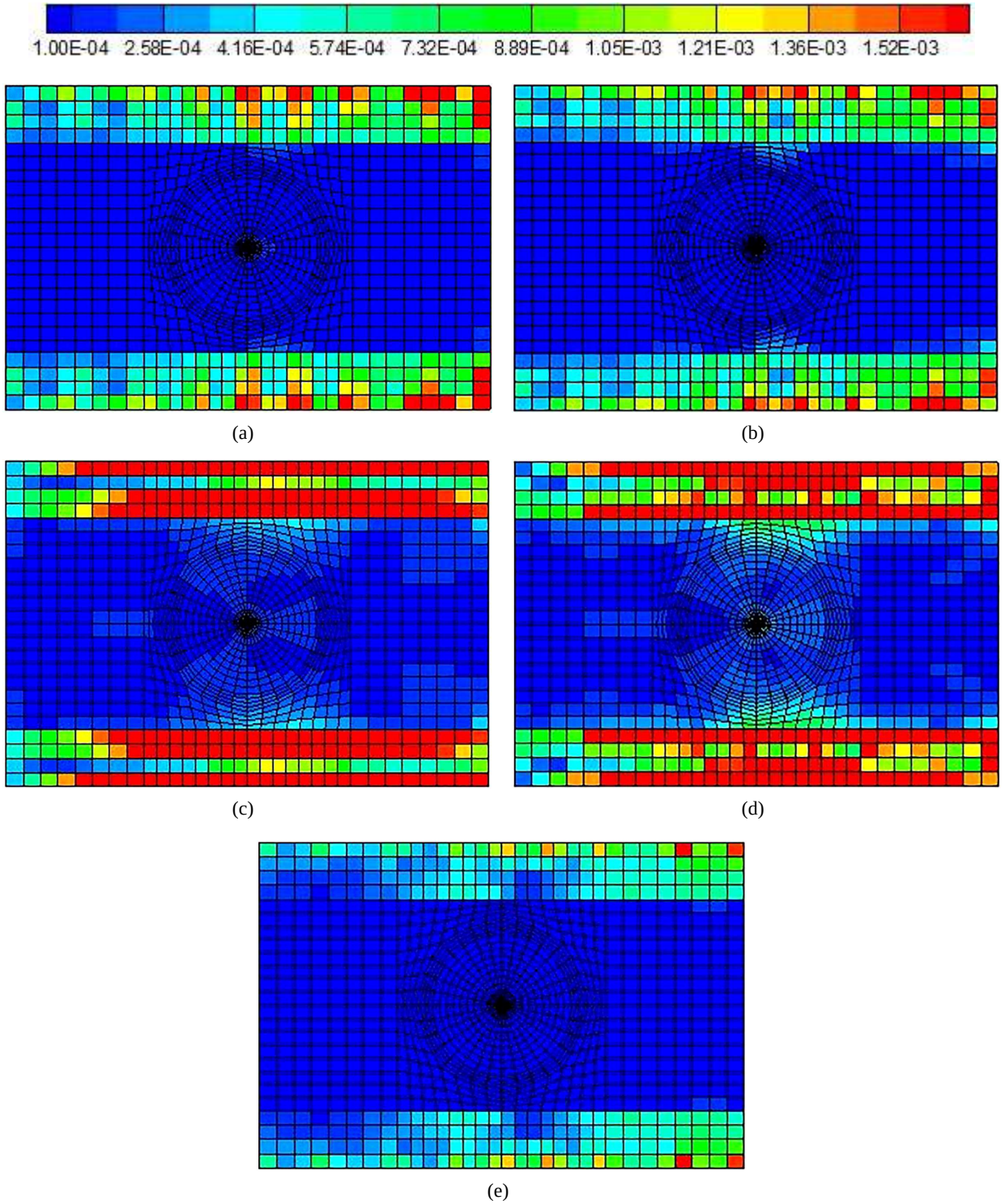

FIG. 6: Tensile loading case: error map $\eta^{e,L}$ from various methods: (a) L^2 coupling–linear weighting function, (b) H^1coupling–linear weighting function, (c) H^1 coupling–constant weighting function ($\alpha^L = 0.99$), (d) H^1 coupling–constant weighting function ($\alpha^L = 0.5$), and (e) s-method

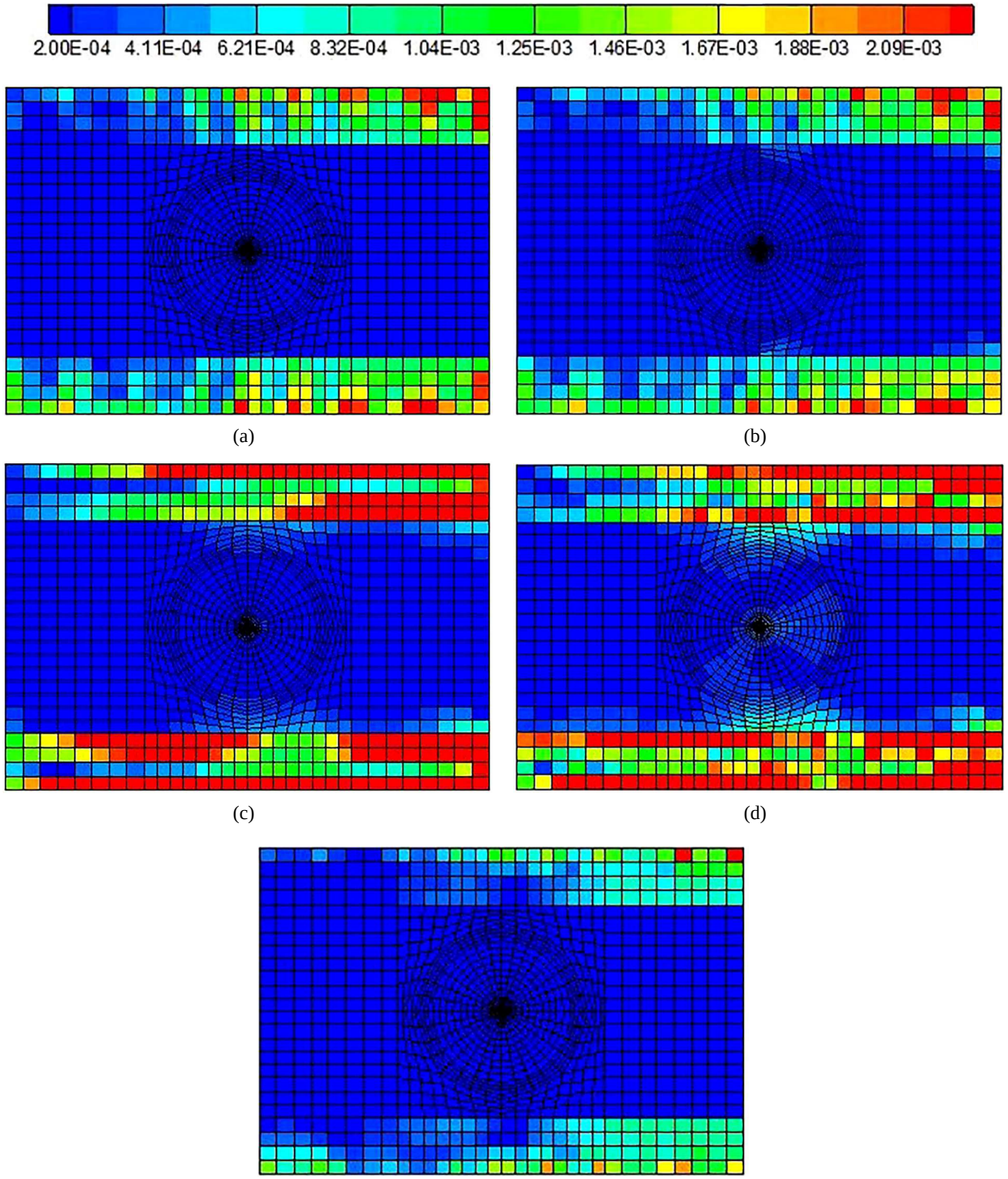

FIG. 7: Shear loading case: error map $\eta^{e,L}$ from various methods: (a) L^2 coupling–linear weighting function, (b) H^1 coupling–linear weighting function, (c) H^1 coupling–constant weighting function ($\alpha^L = 0.99$), (d) H^1 coupling–constant weighting function ($\alpha^L = 0.5$), and (e) s-method

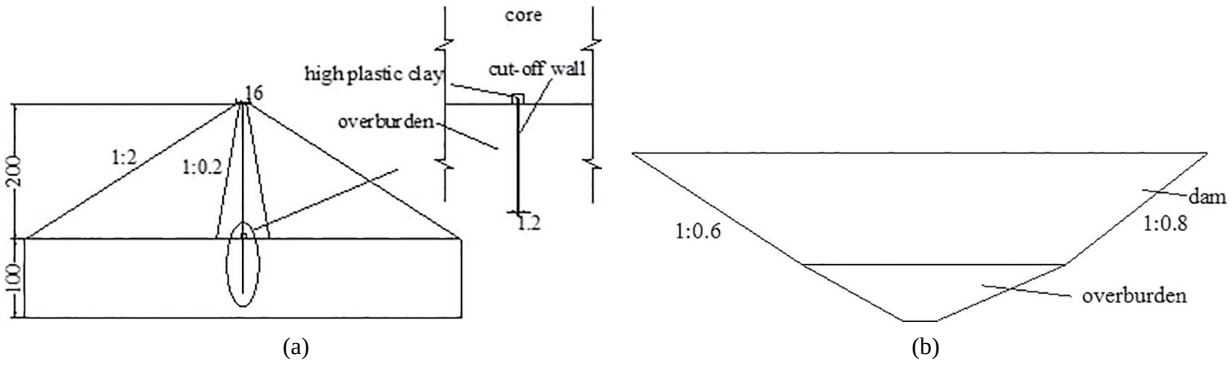

FIG. 8: High earth-rockfill dam with deep overburden and its cutoff wall (unit: m): (a) maximum cross section and (b) maximum longitudinal section

TABLE 4: Material parameters

Material	Saturated Unit Weight (g/cm^3)	c (KPa)	φ (deg)	Duncan-ev Parameters							Yield Stress (KPa)	Elastic Modulus (KPa)	Passion's Ratio
				K	n	R_f	G	F	D	K_{ur}			
Soil	2.3	0	45	1050	0.37	0.71	0.3	0.09	5.8	2100	—	—	—
Core	2.22	35	33	447	0.4	0.75	0.39	0.05	1.9	900	—	—	—
Overburden	1.99	50	34	800	0.43	0.73	0.44	0.1	2	1500	—	—	—
Thin Layer	1.2	3	10	100	0.45	0.5	0.3	0.04	0.50	150	—	—	—
High Plastic Clay	1.55	39	23	110	0.46	0.88	0.46	0.18	1	220	—	—	—
Cutoff Wall	2.5	2000	48	—	—	—	—	—	—	—	20,000	3×10^7	0.167

The distributions of stress (stress positive in tension), force, and moment of the cutoff wall along the depth for different models are shown in Fig. 10. Assuming that the fine mesh results are almost exact, we can make several observations: (i) the Arlequin provides added accuracy over the coarse mesh but is considerably less accurate than the s-method, in particular, in predicting the maximum compressive stress and (ii) in terms of computational efficiency, both methods provide considerable savings over the fine mesh with the cost of the s-method and Arlequin method being 20 and 24% of the fine mesh cost (see Table 5), respectively.

4. DISCUSSIONS

In this section, we explain the reasons for superior precision of the s-method, when used with the given local and global meshes to approximate the problems considered in the previous section. We first show in Section 4.1 that the exact solution of the single domain problem $\boldsymbol{u}^*$ can be recovered by both the s-method and Arlequin method, which proves the so-called consistency of the two methods. However, once the spatial discretization is introduced, both methods are expected to have discretization error. The difference in accuracy between the s-method and Arlequin method in solving the problems considered herein is explained in Section 4.2.

4.1 Consistency of the Two Methods with the Single Domain Model

Consider the multidomain problem in Fig 1. For simplicity, attention is restricted to elastic body, such that, Eq. (6) becomes

$$\sigma = \mathbb{L} : \varepsilon \quad \text{in} \quad \Omega \tag{71}$$

where $\mathbb{L}$ is the linear constitutive tensor.

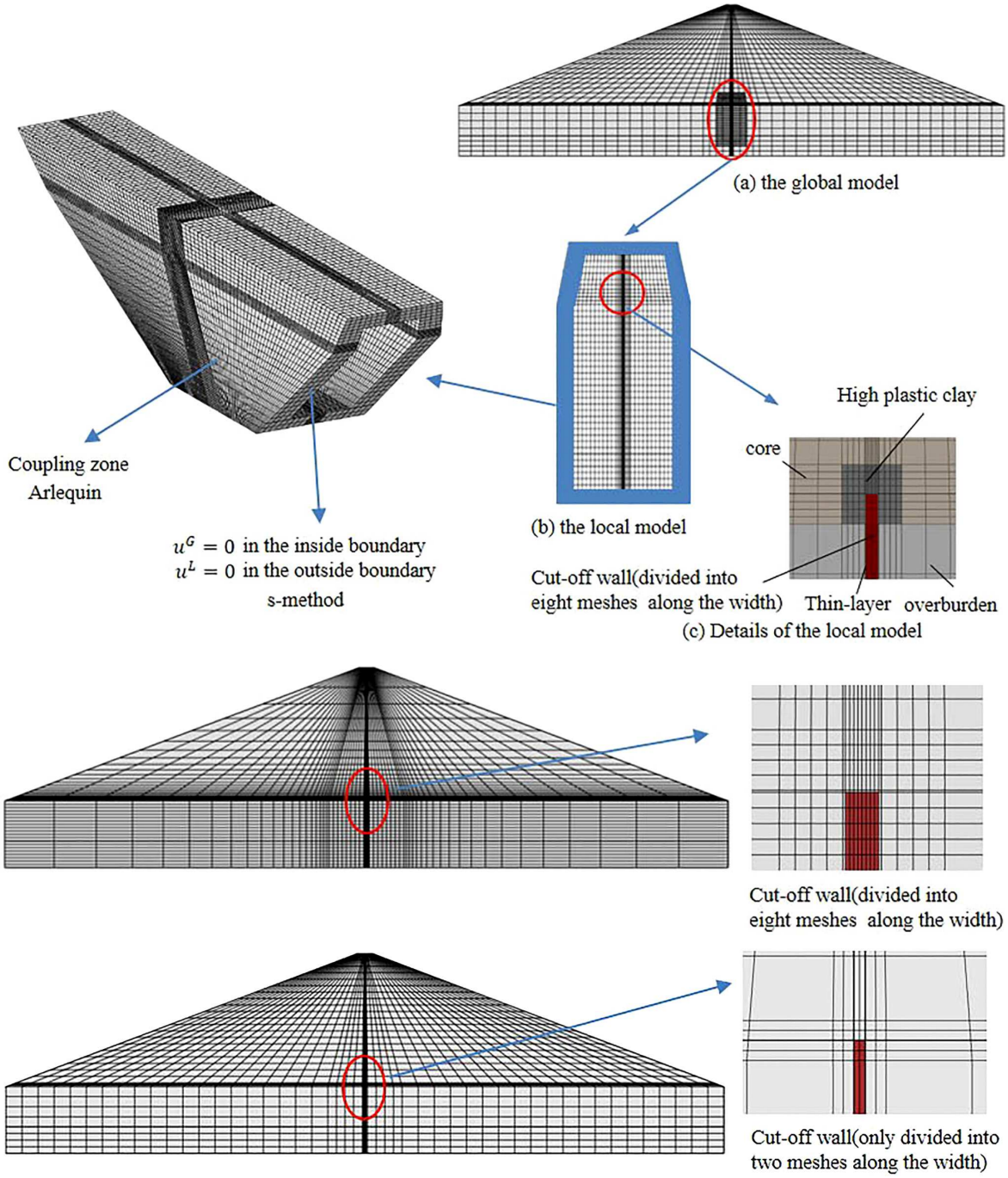

FIG. 9: Various meshes of the multiscale analysis of the cutoff wall: (a) s-method and Arlequin model, (b) fine model, and (c) coarse model

Ben Dhia (2008) proved the proposition that the solution of the linear elasticity single domain problem can be recovered by the Arlequin solutions. Herein, we give a similar proof for the variant of the s-method.

Let $\boldsymbol{u}^S$ defined by

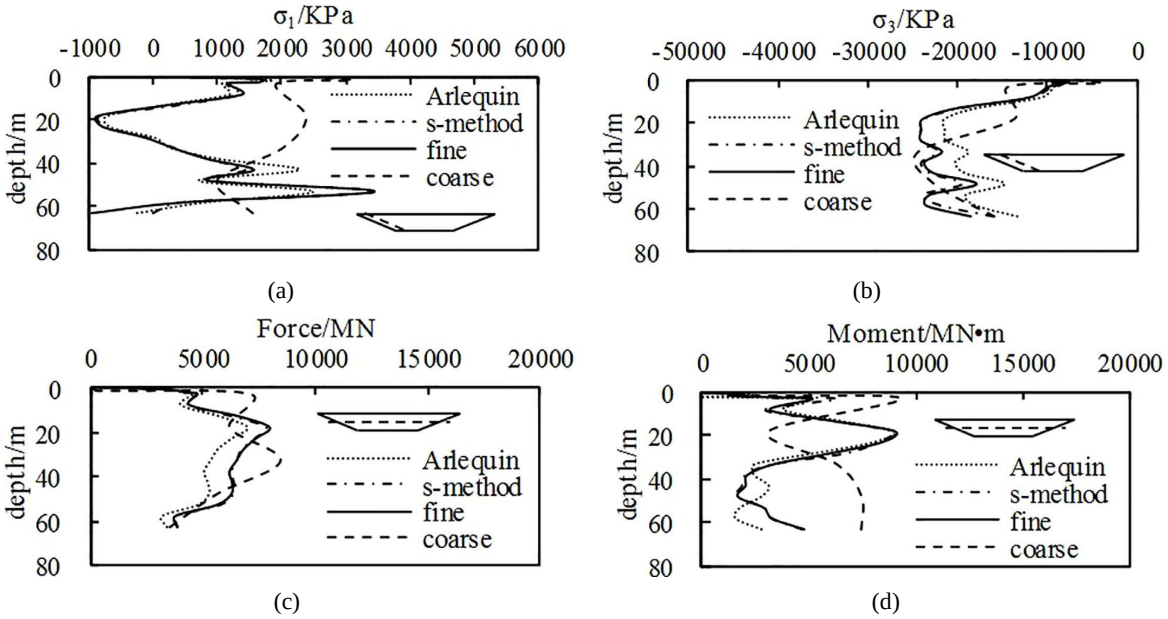

FIG. 10: Results from various methods

TABLE 5: Computational efficiency of the various methods

	Elements	Nodes	Degrees of Freedom		CPU Times	
			Value	Normalized Value to the Fine Mesh	Value/s	Normalized Value to the Fine Mesh
s-Method	212,800	231,329	693,987	0.54	181,329	0.20
Arlequin	265,344	236,033	708,099	0.55	215,491	0.24
Fine	411,952	429,633	1,288,899	—	915,939	—
Coarse	91,392	97,755	293,265	—	21,104	—

$$\boldsymbol{u}^S = \begin{cases} \boldsymbol{u}^G & \text{in} \quad \Omega^G/\Omega^0 \\ \boldsymbol{u}^G + \boldsymbol{u}^L & \text{in} \quad \Omega^0 \\ \boldsymbol{u}^L & \text{in} \quad \Omega^L/\Omega^0 \end{cases} \tag{72}$$

be the solution of Eq. (16). The proposition that $\boldsymbol{u}^S = \boldsymbol{u}^*$ in Ω is proved in two steps. First, we show that $\boldsymbol{u}^S$ is a unique solution of Eq. (16). Setting $\boldsymbol{u}^S = \boldsymbol{u}^*$, it is a trivial exercise to show that $\boldsymbol{u}^*$ is the solution of Eq. (16). Now assume that there are two solutions $\boldsymbol{u}_1^S$, $\boldsymbol{u}_2^S$ of Eq. (16). By choosing $\boldsymbol{u}_1^S - \boldsymbol{u}_2^S$ as a virtual field, one deduces that

$$\int_\Omega \boldsymbol{\varepsilon}(\boldsymbol{u}_1^S - \boldsymbol{u}_2^S) : \mathbb{L} : \boldsymbol{\varepsilon}(\boldsymbol{u}_1^S - \boldsymbol{u}_2^S) d\Omega = 0 \tag{73}$$

and since $\mathbb{L}$ is a positive definite, it follows that $\boldsymbol{u}_1^S = \boldsymbol{u}_2^S \equiv \boldsymbol{u}^S$.

In the second step we show that $\boldsymbol{u}^S = \boldsymbol{u}^*$. Consider the virtual displacement $\boldsymbol{v}^S$ defined as as follows:

$$\boldsymbol{v}^S = \begin{cases} \boldsymbol{v}^G & \text{in} \quad \Omega^G/\Omega^0 \\ \boldsymbol{v}^G + \boldsymbol{v}^L & \text{in} \quad \Omega^0 \\ \boldsymbol{v}^L & \text{in} \quad \Omega^L/\Omega^0 \end{cases} \tag{74}$$

to be an element of $\mathcal{V}$, i.e., $\boldsymbol{v}^S \in \mathcal{V}$. We then construct $\boldsymbol{v}^S$ as follows:

$$\boldsymbol{v}^S = \begin{cases} \boldsymbol{v}^*|_{\Omega^G/\Omega^0} \\ \boldsymbol{v}^*|_{\Omega^0} \\ \boldsymbol{v}^*|_{\Omega^L/\Omega^0} \end{cases} \tag{75}$$

where $\boldsymbol{v}^*$ is an element in $\mathcal{V}$.

Inserting (75) into (16), and due to the uniqueness of the elasticity problem, yields

$$\boldsymbol{u}^S = \boldsymbol{u}^* \quad \text{in} \quad \Omega \tag{76}$$

which completes the proof.

Remark 2. *Solving problem in Eqs. (16)–(18) amounts to finding out local and global solutions, defined in their respective domains, whose sum gives the solution $\boldsymbol{u}^S$, which, as shown above, is unique. Of course, one can note that there is an infinity of possible solutions $\boldsymbol{u}^G$, $\boldsymbol{u}^L$ in the overlap whose sum gives the same unique solution $\boldsymbol{u}^S$, in the overlap. However, once the spatial discretization is introduced, at least for the structured mesh superposition considered herein, the non-uniqueness issue (Fish, 1992a; Fish and Markolefas, 1993; Jiao, 2015a,b) can be remedied by constraining the global mesh nodes that coincide with local mesh nodes in the interior of the overlap to solve the discreet redundancy issue. We refer also to the Tiling method (Seroussi et al., 2012), introduced for the coupling of different ice models of different order complexity where a similar redundancy issue is treated by using a single layer of elements in the overlap.*

4.2 The Modelling Error with Respect to Discrete Single Domain Model

The difference of accuracy of modeling error results obtained in the previous sections with a variant of the s-method and Arlequin method is explained in this section. The main point is linked to the approximation precision in the overlap zone that could be expected from the two approaches, for a fixed discretization since in the complementary domains, the same numerical models are used by both of them.

With the variant of the s-method, the unique solution $\boldsymbol{u}^*$ of the continuous classical single model problem is approximated, in the overlap, by the enrichment of the fine FE solution of the coarse FE solution and suppression of redundant basis elements. This results in an approximation almost similar to the single FE model.

With the Arlequin method, it can be easily shown that the coupling operator [third system in Eq. (40)] used to enforce the weak equality between the global coarse solution $\boldsymbol{u}^G$ and the local solution $\boldsymbol{u}^L$, in the overlap Ω^0, leads to the enforcement of the equality between $\boldsymbol{u}^G$ and the orthogonal projection of $\boldsymbol{u}^L$ on the global coarse space (see, Ben Dhia and Rateau, 2005). Thus, the solution $\boldsymbol{u}^*$ of the continuous single model problem, in the overlap, is approximated by a partition of the global coarse part and the fine part of the Arlequin problem solution, the latter being constrained to have its projection on the coarse space equal to coarse part. This leads to an Arlequin approximation in the overlap that is richer than the coarse part but poorer than the fine part. Alternatively, if the fine space is used as the mediator space of Lagrange multipliers in the Arlequin method, the coupling operator would have enforced the exact equality between the local and global fields in the overlap. This would have led to an approximation of $\boldsymbol{u}^*$ in Ω^0, in the coarse FE space restricted to Ω^0. Thus, for both of these two classical choices, if the global FE coarse part of the Arlequin solution is not able to capture with a required precision the solution $\boldsymbol{u}^*$ in Ω^0, modeling errors are automatically generated in the overlap (see Figs. 6 and 7) and pollution errors are diffused in the zone of interest.

5. CONCLUSIONS

A variant of the s-method as an alternative scheme to the concurrent coupling has been developed and compared to the Arlequin method. The proposed primal method is inspired by a combination of s-version of the finite element method and the Arlequin method. For the example problems considered, the new variant of the s-method is found to be more accurate than the Arlequin approach and offers minor computational cost savings. The cause of accuracy

gains is explained in this work. It is linked to the approximation of the continuous solution in the overlap by both methods and used global coarse discretization in this zone: the s-method uses a finer approximation of the solution in the overlap (almost as fine as the classical single fine model). A recommendation for the choice of the Arlequin coupling/gluing zone (see, Ben Dhia and Rateau, 2002) is that the latter has to be a part of the domain of regularity, where the used "coarse" approximation leads to a targeted accuracy. In general, this could be achieved by model adaptivity algorithms (see, e.g., Ben Dhia et al., 2011).

Future work will focus on coupling different mathematical models as well as wave propagation problems.

ACKNOWLEDGMENT

Author Wei Sun thanks the Chinese Scholarship Council (CSC) (Grant No. 201760210218) for providing the funding that enabled him to visit Columbia University to do the work presented in this paper.

REFERENCES

Bauman, P.T., Ben Dhia, H., Elkhodja, N., Oden, J.T., and Prudhomme, S., On the Application of the Arlequin Method to the Coupling of Particle and Continuum Models, *Comput. Mech.*, vol. **42**, no. 4, pp. 511–530, 2008.

Belgacem, F.B., The Mortar Finite Element Method with Lagrange Multipliers, *Numer. Math.*, vol. **84**, no. 2, pp. 173–197, 1999.

Belytschko, T. and Black, T., Elastic Crack Growth in Finite Elements with Minimal Remeshing, *Int. J. Numer. Methods Eng.*, vol. **45**, no. 5, pp. 601–620, 1999.

Belytschko, T., Liu, W.K., Moran, B., and Elkhodary, K.I., *Nonlinear Finite Elements for Continua and Structures*, 2nd Ed., Hoboken, NJ: Wiley, 2014.

Ben Dhia, H. and Elkhodja, N., Coupling Atomistic and Continuum Models in the Arlequin Framework, *Proc. 8ème Congrès de Mécanique Marocain*, April, El Jadida, Morocco, pp. 133–135, 2007.

Ben Dhia, H. and Rateau, G., Application of the Arlequin Method to Some Structures with Defects, *Revue Européenne des Éléments Finis*, vol. **11**, nos. 2-4, pp. 291–304, 2002.

Ben Dhia, H. and Rateau, G., Mathematical Analysis of the Mixed Arlequin Method, *Comptes Rendus Acad. Sci. Paris Série I*, vol. **332**, pp. 649–654, 2001.

Ben Dhia, H. and Rateau, G., The Arlequin Method as a Flexible Engineering Design Tool, *Int. J. Numer. Methods Eng.*, vol. **62**, no. 11, pp. 1442–1462, 2005.

Ben Dhia, H., Chamoin, L., Oden, J.T., and Prudhomme, S., A New Adaptive Modeling Strategy based on Optimal Control for Atomic-to-Continuum Coupling Simulations, *Comput. Methods Appl. Mech. Eng.*, vol. **200**, nos. 37-40, pp. 2675–2696, 2011.

Ben Dhia, H., Elkhodja, N., and Roux, F.-X., Multimodeling of Multi-Alterated Structures in the Arlequin Framework Solution with a Domain-Decomposition Solver, *Euro. J. Comput. Mech.*, vol. **17**, pp. 969–980, 2008.

Ben Dhia, H., Further Insights by Theoretical Investigations of the Multiscale Arlequin Method, *Int. J. Multiscale Comput. Eng.*, vol. **6**, no. 3, pp. 1–18, 2008.

Ben Dhia, H., Multiscale Mechanical Problems: The Arlequin Method, *Comptes Rendus Acad. Sci. Série IIb*, vol. **326**, pp. 899–904, 1998.

Ben Dhia, H., Numerical Modelling of Multiscale Problems: The Arlequin Method, in *CD Proc. ECCM'99*, Munchen, 1999.

Bernardi, C., Debit, N., and Maday, Y., Coupling Finite Element and Spectral Methods: First Results, *Math. Comput.*, vol. **54**, no. 189, pp. 21–39, 1990a.

Bernardi, C., Maday, Y., and Patera, A.T., A New Nonconforming Approach to Domain Decomposition: The Mortar Element Method, Collège de France Seminar, Pitman, H. Brezis and J.-L. Lions, Eds., Pitman, 1990b.

Duncan, J.M. and Zhang, C.Y., Nonlinear Analysis of Stress and Strain in Soils, *J. Soil Mech. Found. Div.*, vol. **96**, pp. 1629–1653, 1970.

Duval, M., Passieux, J.-C., Salaün, M., and Guinard, S., Non-Intrusive Coupling: Recent Advances and Scalable Nonlinear Domain Decomposition, *Arch. Comput. Methods Eng.*, vol. **23**, no. 1, pp. 17–38, 2016.

Fan, R. and Fish, J., The rs-Method for Material Failure Simulations, *Int. J. Numer. Methods Eng.*, vol. **73**, no. 11, pp. 1607–1623, 2008.

Farhat, C. and Roux, F.-X., A Method of Finite Element Tearing and Interconnecting and Its Parallel Solution Algorithm, *Int. J. Numer. Methods Eng.*, vol. **32**, no. 6, pp. 1205–1227, 1991.

Feyel, F., Multiscale FE^2 Elastoviscoplastic Analysis of Composite Structures, *J. Comput. Mater. Sci.*, vol. **16**, nos. 1-4, pp. 344–354, 1999.

Fish, J. and Shek, K., Multiscale Analysis of Composite Materials and Structures, *Compos. Sci. Technol.*, vol. **60**, nos. 12-13, pp. 2547–2556, 2000.

Fish, J. and Markolefas, S., Adaptive s-Method for Linear Elastostatics, *Comput. Methods Appl. Mech. Eng.*, vol. **104**, no. 3, pp. 363–396, 1993.

Fish, J., Bridging the Scales in Nano Engineering and Science, *J. Nanopart. Res.*, vol. **8**, no. 5, pp. 577–594, 2006.

Fish, J., Hierarchical Modelling of Discontinuous Fields, *Int. J. Numer. Methods Eng.*, vol. **8**, no. 7, pp. 443–453, 1992b.

Fish, J., Nuggehally, M.A., Shephard, M.S., Picu, C.R., Badia, S., Parks, M.L., and Gunzburger, M., Concurrent AtC Coupling based on a Blend of the Continuum Stress and the Atomistic Force, *Comput. Methods Appl. Mech. Eng.*, vol. **196**, nos. 45-48, pp. 4548–4560, 2007.

Fish, J., *Practical Multiscaling*, Hoboken, NJ: Wiley, 2013.

Fish, J., Suvorov, A., and Belsky, V., Hierarchical Composite Grid Method for Global-Local Analysis of Laminated Composite Shells, *Appl. Numer. Math.*, vol. **23**, no. 2, pp. 241–258, 1997.

Fish, J., The s-Version of the Finite Element Method, *Comput. Struct.*, vol. **43**, no. 3, pp. 539–547, 1992a.

Fish, J., Yu, Q., and Shek, K., Computational Damage Mechanics for Composite Materials based on Mathematical Homogenization, *Int. J. Numer. Methods Eng.*, vol. **45**, no. 11, pp. 1657–1679, 1999.

Gendre, L., Allix, O., Gosselet, P., and Comte, F., Non-Intrusive and Exact Global/Local Techniques for Structural Problems with Local Plasticity, *Comput. Mech.*, vol. **44**, no. 2, pp. 233–245, 2009.

Guidault, P.A. and Belytschko, T., On the L^2 and the H^1 Couplings for an Overlapping Domain Decomposition Method using Lagrange Multipliers, *Int. J. Numer. Methods Eng.*, vol. **70**, no. 3, pp. 322–350, 2007.

Guo, N. and Zhao, J., A Coupled FEM/DEM Approach for Hierarchical Multiscale Modelling of Granular Media, *Int. J. Numer. Methods Eng.*, vol. **99**, no. 11, pp. 789–818, 2014.

HKS, *ABAQUS/Standard User's Manual*, Hibbitte, Karlsson, Sorenson, Inc., 2002.

Hughes, T.J., Multiscale Phenomena: Green's Functions, the Dirichlet-to-Neumann Formulation, Subgrid Scale Models, Bubbles and the Origins of Stabilized Methods, *Comput. Methods Appl. Mech. Eng.*, vol. **127**, nos. 1-4, pp. 387–401, 1995.

Jiao, Y. and Fish, J., Adaptive Delamination Analysis, *Int. J. Numer. Methods Eng.*, vol. **104**, no. 11, pp. 1008–1037, 2015a.

Jiao, Y. and Fish, J., On the Equivalence between the s-Method, the XFEM and the Ply-by-Ply Discretization for Delamination Analyses of Laminated Composites, *Int. J. Fract.*, vol. **191**, nos. 1-2, pp. 107–129, 2015b.

Melenk, J.M. and Babuška, I., The Partition of Unity Finite Element Method: Basic Theory and Applications, *Comput. Methods Appl. Mech. Eng.*, vol. **139**, nos. 1-4, pp. 289–314, 1996.

Mota, A., Tezaur, I., and Alleman, C., The Schwarz Alternating Method in Solid Mechanics, *Comput. Methods Appl. Mech. Eng.*, vol. **319**, pp. 19–51, 2017.

Qiao, H., Yang, Q.D., Chen, W.Q., and Zhang, C.Z., Implementation of the Arlequin Method into ABAQUS: Basic Formulations and Applications, *Adv. Eng. Soft.*, vol. **42**, no. 4, pp. 197–207, 2011.

Schwarz, H., Uber Einen Grenz Ubergang durch Alternierendes, *Verfahren Vierteljahrsschr. Naturforschenden Ges. Zurich*, vol. **15**, pp. 272–286, 1870.

Seroussi H., Ben Dhia, H., Morlighem, M., Larour, E., Rignot, E., and Aubry, D., Coupling Ice Flow Models of Varying Orders of Complexity with the Tiling Method, *J. Glaciol.*, vol. **58**, no. 210, pp. 776–786, 2012.

Simo, J.C. and Hughes, T.J.R., *Computational Inelasticity*, New York, NY: Springer Science and Business Media, 2006.

Strouboulis, T., Babuška, I., and Copps, K., The Design and Analysis of the Generalized Finite Element Method, *Comput. Methods Appl. Mech. Eng.*, vol. **181**, nos. 1-3, pp. 43–69, 2000.

Sun, W. and Mota, A., A Multiscale Overlapped Coupling Formulation for Large-Deformation Strain Localization, *Comput. Mech.*, vol. **54**, no. 3, pp. 803–820, 2014.

Xiao, S.P. and Belytschko, T., A Bridging Domain Method for Coupling Continua with Molecular Dynamics, *Comput. Meth. Appl. Mechods Eng.*, vol. **193**, nos. 17-20, pp. 1645–1669, 2004.

Xu, M. and Belytschko, T., Conservation Properties of the Bridging Domain Method for Coupled Molecular/Continuum Dynamics, *Int. J. Numer. Methods Eng.*, vol. **76**, no. 3, pp. 278–294, 2008.

APPENDIX A. PROGRAM IMPLEMENTATION FOR THE S-METHOD AND ARLEQUIN METHOD IN ABAQUS

Herein we describe nonlinear s-method and Arlequin program implementations in ABAQUS (HKS, 2002) by combining UEL (user element subroutine), UMAT (user material subroutine), and UVARM (user element output subroutine), as shown in Fig. A.1. The preprocessing C and MATLAB scripts are used to specify relations of nodes and elements in the coupling zone and generate input files automatically. The Lagrange multipliers or the interaction stiffness

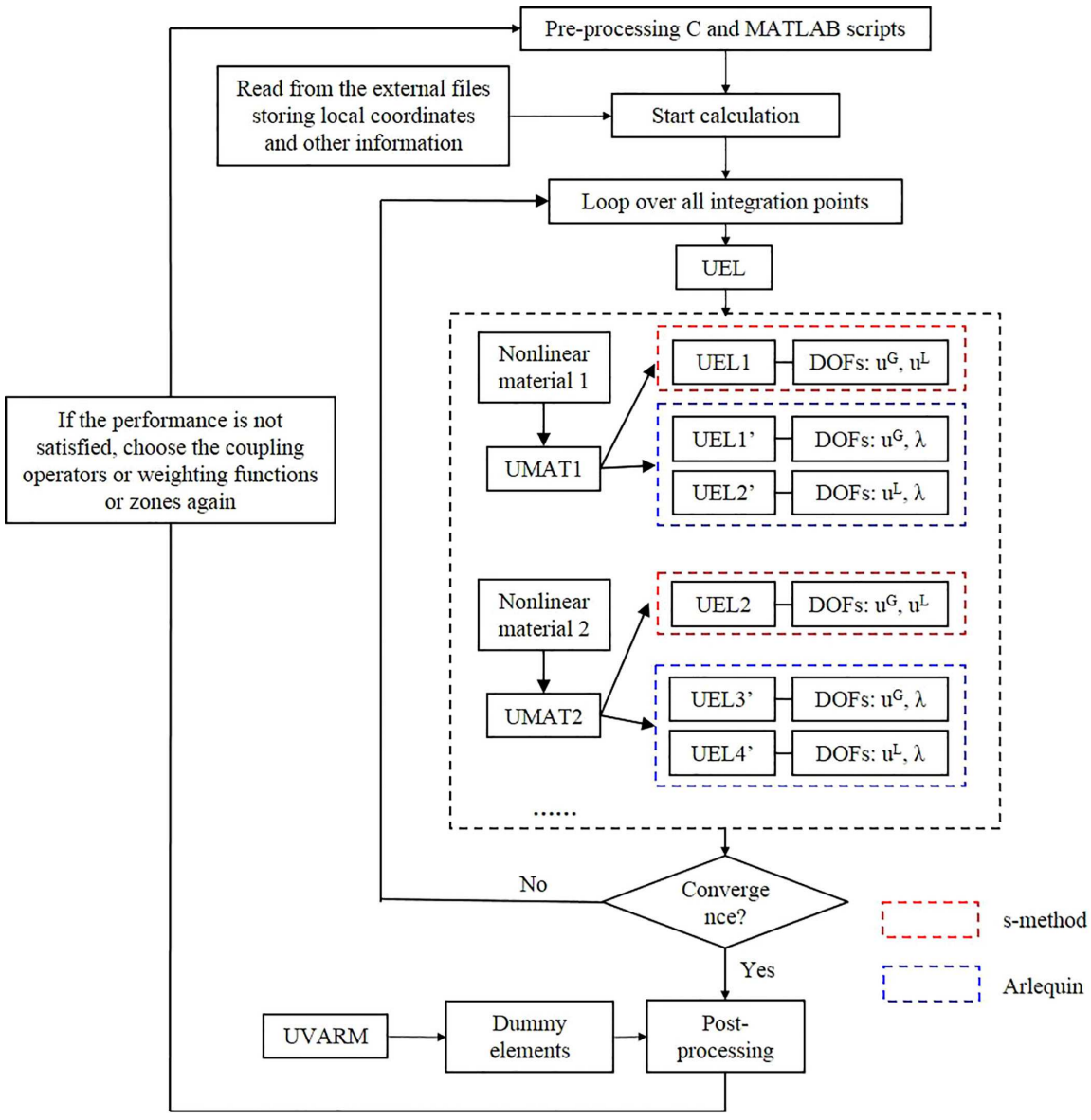

FIG. A.1: Flow chart of the nonlinear Arlequin method and s-method program

matrices were introduced by UEL. The constitutive material models are implemented in UMAT. The updated stress and internal state variables (Belytschko, 2014; Simo, 2006) in UMAT are passed to UEL to compute the tangent stiffness matrix. The postprocessing operations are based on UVARM, i.e., using dummy elements with negligible stiffness that coincide with the position of UEL elements.

For the s-method, the UEL1 (user elements 1) structure is

$$\text{AMATRIX}_{\text{UEL1}} = \begin{bmatrix} (\boldsymbol{K}^{GG})^e & (\boldsymbol{K}^{GL})^e \\ (\boldsymbol{K}^{LG})^e & (\boldsymbol{K}^{LL})^e \end{bmatrix} \tag{A.1}$$

In the Arlequin method, two UELs are employed UEL1′ (user elements 1′), UEL2′ (user elements 2′), which are composed of the coarse-mesh nodes and virtual nodes, as well as fine-mesh nodes and virtual nodes, respectively

$$\text{AMATRIX}_{\text{UEL1}} = \begin{bmatrix} (\alpha^G \boldsymbol{K}^{GG})^e & (\boldsymbol{C}^{G\lambda})^e \\ [(\boldsymbol{C}^{G\lambda})^T]^e & 0 \end{bmatrix} \tag{A.2}$$

$$\text{AMATRIX}_{\text{UEL2}} = \begin{bmatrix} (\alpha^L \boldsymbol{K}^{LL})^e & -(\boldsymbol{C}^{L\lambda})^e \\ -[(\boldsymbol{C}^{L\lambda})^T]^e & 0 \end{bmatrix} \tag{A.3}$$